# A Novel Allosteric Inhibitor of the Uridine Diphosphate N-Acetylglucosamine Pyrophosphorylase from Trypanosoma brucei

Michael D. Urbaniak,[†] Iain T. Collie,[†] Wenxia Fang,[‡] Tonia Aristotelous,[†] Susanne Eskilsson,[†] Olawale G. Raimi,[‡] Justin Harrison,[†] Iva Hopkins Navratilova,[†] Julie A. Frearson,[†] Daan M. F. van Aalten,[‡,§] and Michael A. J. Ferguson*,[†]

[†]Division of Biological Chemistry and Drug Discovery, [‡]Division of Molecular Microbiology, and [§]MRC Protein Phosphorylation and Ubiquitylation Unit, College of Life Sciences, University of Dundee, Dundee DD1 5EH, U.K.

ⓢ *Supporting Information*

ABSTRACT: Uridine diphosphate N-acetylglucosamine pyrophosphorylase (UAP) catalyzes the final reaction in the biosynthesis of UDP-GlcNAc, an essential metabolite in many organisms including *Trypanosoma brucei*, the etiological agent of Human African Trypanosomiasis. High-throughput screening of recombinant *T. brucei* UAP identified a UTP-competitive inhibitor with selectivity over the human counterpart despite the high level of conservation of active site residues. Biophysical characterization of the UAP enzyme kinetics revealed that the human and trypanosome enzymes both display a strictly ordered bi−bi mechanism, but with the order of substrate binding reversed. Structural characterization of the *T. brucei* UAP−inhibitor complex revealed that the inhibitor binds at an allosteric site absent in the human homologue that prevents the conformational rearrangement required to bind UTP. The identification of a selective inhibitory allosteric binding site in the parasite enzyme has therapeutic potential.
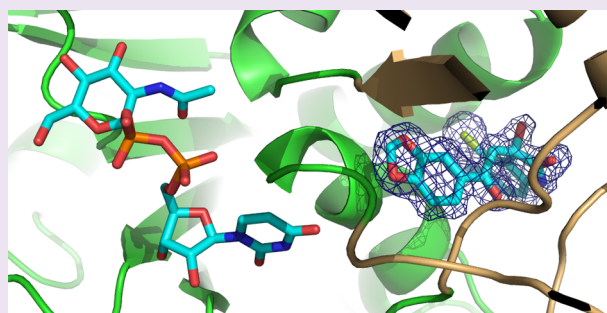
The sugar nucleotide uridine diphosphate N-acetylglucosamine (UDP-GlcNAc) is an important and ubiquitous metabolite that is used in eukaryotes as the source of N-acetylglucosamine in the biosynthesis of N-linked and O-linked glycans and the source of glucosamine in glycosylphosphatidylinositol anchors. In addition, UDP-GlcNAc is required for the formation of lipopolysaccharide and peptidoglycans used in bacterial cell wall biosynthesis and the formation of chitin for fungal cell wall biosynthesis. The enzyme UDP-GlcNAc pyrophosphorylase (UAP) is responsible for a key transformation in the biosynthesis of UDP-GlcNAc by catalyzing the reversible reaction between UTP and glucosamine-1-phosphate (Glc-1-P) forming UDP-GlcNAc and inorganic pyrophosphate (PP$_i$) (Scheme 1). The enzyme represents a bottleneck between different glycoconjugate biosynthetic pathways that has the potential to be exploited as a therapeutic target, provided that species-specific inhibitors can be found.

Trypanosoma brucei is a protozoan parasite transmitted by the bite of an infected tsetse fly (*Glossina* spp.) and is the etiological agent of Human African Trypanosomiasis (HAT, also known as African sleeping sickness). The disease is responsible for 10,000 recorded deaths per annum in sub-Saharan Africa, although due to poor surveillance the true number is estimated to be much higher.[1] Current treatments are expensive, toxic, and difficult to deliver, leaving an urgent unmet need for improved therapeutic agents.[2] The parasite has a digenetic lifecycle between a mammalian host and insect vector and produces a complex array of glycoconjugates, some of which are essential for its

infectivity and virulence. Several enzymes involved in the biosynthesis of glycosylphosphatidylinositol anchors[3−5] and sugar nucleotide biosynthesis[6−10] have been shown to be essential in bloodstream form *T. brucei* by genetic validation.

T. brucei UAP (*Tb*UAP) has been genetically validated in bloodstream form parasites as essential both *in vitro* and *in vivo* and has been proposed as a potential therapeutic target, although selective inhibition of the parasite UAP would be a therapeutic requirement.[8] Despite the moderate level of overall sequence similarity between *Tb*UAP and its human counterpart (31% sequence identity, 50% sequence similarity), only two of the 15 identified substrate-interacting residues in human UAP (*Hs*UAP) are different,[8,11] and there are no known inhibitors of UAP. In this work we set out to discover novel species-specific inhibitors of *Tb*UAP through high-throughput screening of the recombinant enzyme. Through biophysical and structural characterization, we reveal that the trypanosome and human UAP differ in the order of sequential substrate binding and that a primary hit compound is a species-specific UTP-competitive allosteric inhibitor of *Tb*UAP.

■ RESULTS AND DISCUSSION

Identification of Novel TbUAP Inhibitors. Recombinant *T. brucei* UAP (*Tb*UAP) was screened against a diverse library of

Scheme 1. Enzyme-Catalyzed Formation of UDP-GlcNAc[a]
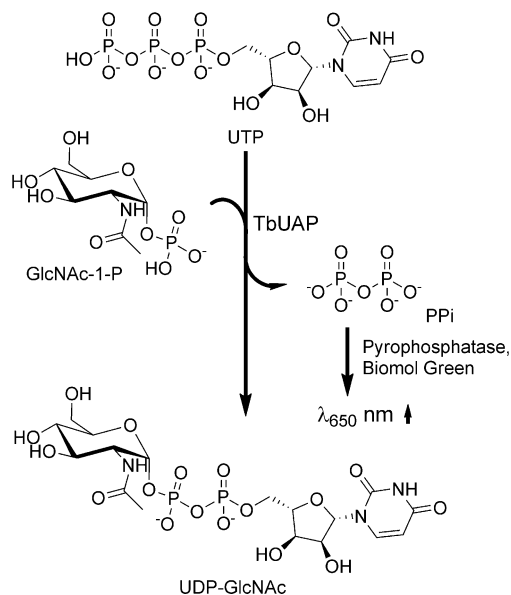
[a]The substrates UTP and GlcNAc-1-P are combined to form the products UDP-GlcNAc and inorganic pyrophosphate. The reaction can be monitored with pyrophosphatase that converts the inorganic pyrophosphate to phosphate, and addition of BIOMOL Green reagent results in an increase in absorption at 650 nm due to the formation of a malachite green/molybdate complex.

63,362 molecules using a discontinuous coupled colorimetric assay that monitors phosphate generation (Scheme 1).[8] The initial 73 hit compounds that showed >25% inhibition at 30 μM (0.12% hit rate) were triaged by removing compounds that displayed activity against the *E. coli* pyrophosphatase coupling enzyme. The 12 remaining compounds were all confirmed as *Tb*UAP inhibitors by direct monitoring of their effects on conversion of the substrate (UTP) to product (UDP-GlcNAc) by HPLC. Their IC$_{50}$ values were determined using the coupled assay. Commercially available analogues of the two most potent compounds, **1** and **2** (Scheme 2, IC$_{50}$ = 37 $\pm$ 4 and 49 $\pm$ 4 μM,

Scheme 2. *Tb*UAP Inhibitors Identified by High-Throughput Screening
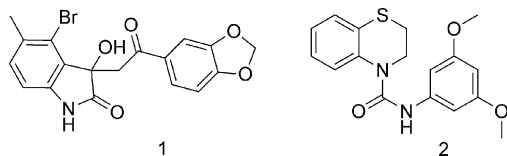
respectively), were identified by substructure searching, and 30 analogues were purchased and assayed for activity. None of the compounds showed improved potency over that of the parent compounds, with the relatively low potencies limiting the derivation of structure−activity relationships.

TbUAP1 Binds Its Substrates in a Different Order from HsUAP1. To examine the enzyme reaction mechanism and explore the mode of action of the most potent inhibitor **1**, a series of surface plasmon resonance (SPR) experiments were employed (Figure 1 and 2, Table 1). The reaction mechanism of UAP requires that both UTP and GlcNAc-1-P bind to the enzyme, but it was unknown if the sequential binding is random or strictly ordered. We examined the binding of the two substrates to
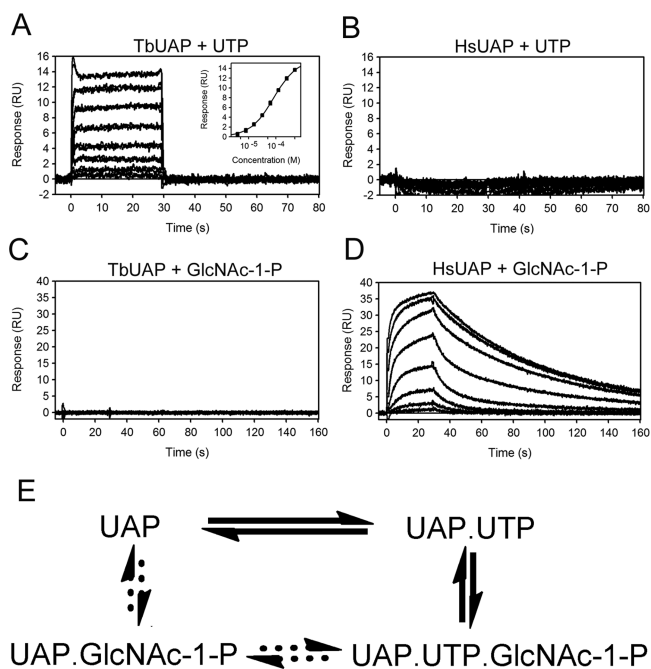

Figure 1. Surface plasmon resonance sensorgrams of *Tb*UAP and *Hs*UAP binding to substrates. (A) *Tb*UAP binds UTP with a K_D of 83.1 $\pm$ 0.5 μM, UTP was injected in duplicates at concentrations from 3.9 to 500 μM. The inset shows an equilibrium affinity fit to a 1:1 binding model. (B) *Hs*UAP does not bind UTP. (C) *Tb*UAP does not bind GlcNAc-1-P. (D) *Hs*UAP binds GlcNAc-1-P with a complex binding profile, GlcNAc-1-P was injected in duplicates at concentrations from 9 nM to 20 μM. (E) The ordered sequential binding of substrates to UAP is reversed between *Tb*UAP (solid arrows) and *Hs*UAP (dashed arrows).

*Tb*UAP and the closest Human homologue UAP-AGX1 (*Hs*UAP) by SPR (Figure 1, Table 1). We found that *Tb*UAP binds UTP alone with a K_D of 83.1 $\pm$ 0.5 μM (K_m = 26 μM, Stokes et al.[8]) but does not bind GlcNAc-1-P alone (K_m = 39 μM, Stokes et al.[8]). In contrast, *Hs*UAP does not bind UTP alone (K_m = 53 μM, Peneff et al.[11]), and although it does show significant binding to GlcNAc-1-P, it was not possible to calculate an affinity due to complex binding kinetics. These data reveal that substrate binding to UAPs is strictly ordered but that, surprisingly, the order of binding is reversed between the two species. To our knowledge this is the first example of species-specificity in sequentially ordered bi−bi mechanisms and raises the intriguing possibility that UTP-competitive inhibitors may confer species specificity.

Compound 1 Is a Competitive Inhibitor of *Tb*UAP1. To investigate the mode of inhibition of **1**, we examined its binding to *Tb*UAP and *Hs*UAP by SPR (Figure 2 and Table 1) and found that it was bound by *Tb*UAP with K_D = 2.58 $\pm$ 0.07 μM, but that *Hs*UAP displayed no significant binding (Figure 2A,B). The binding of **1** to *Tb*UAP was competitive with UTP, with the K_D shifting to K_D = 9.30 $\pm$ 0.1 μM (IC$_{50}$ = 37 $\pm$ 4 μM) in the presence of 500 μM of UTP, while the presence of 100 μM of GlcNAc-1-P did not significantly affect binding with a K_D = 2.35 $\pm$ 0.03 μM (Figure 2D,C). The selectivity observed by SPR was confirmed by testing the activity of **1** against *Tb*UAP and *Hs*UAP in both the coupled assay and HPLC assay, showing consistent inhibition of *Tb*UAP but no significant inhibition of *Hs*UAP (Figure 2E-,F). The coupled assay was used to confirm that inhibition by **1** was competitive with UTP with an apparent K_i of

B

dx.doi.org/10.1021/cb400411x | *ACS Chem. Biol.* XXXX, XXX, XXX−XXX
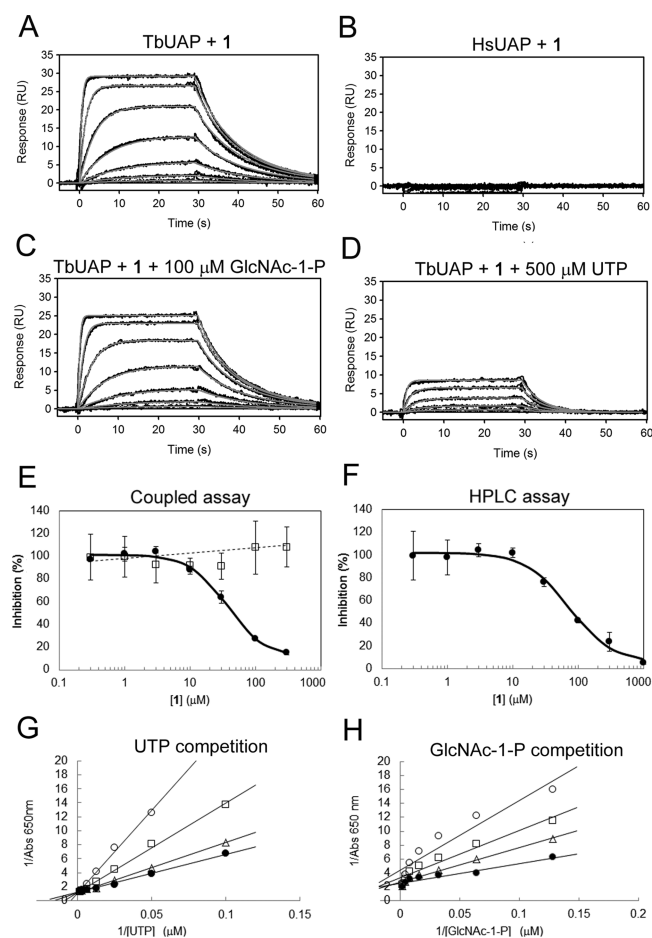
Figure 2. Mode of inhibition by compound **1**. (A) *Tb*UAP binds **1** with a K_D of 2.58 ± 0.07 μM. (B) *Hs*UAP does not bind **1**. (C) The presence of 100 μM Glc-NAc-1-P does not significantly affect the binding of **1** to *Tb*UAP (K_D of 2.35 ± 0.03 μM). Compound **1** was injected in duplicates at a concentration series of 69 nM to 50 μM. (D) The presence of 500 μM UTP competes for the binding of **1** to *Tb*UAP, increasing the K_D to 9.3 ± 0.1 μM and significantly decreasing binding response ($\sim$3-fold). Gray lines represent kinetic fit to 1:1 binding model. (E) Inhibition of *Tb*UAP (closed circles, IC_{50} = 37 ± 4 μM) and *Hs*UAP (open squares, IC_{50} > 1000 μM) in the discontinuous coupled colormetric assay. (F) Inhibition of *Tb*UAP in the direct HPLC assay (IC_{50} = 66 ± 8 μM). (G) Inhibition of *Tb*UAP at varying concentrations of UTP reveals that inhibition is competitive with UTP with an apparent K_i of 60 μM. The concentrations of compound **1** used: open circles 300 μM, open squares 30 μM, open triangles 3 μM, and filled circle 0 μM. (H) Inhibition of *Tb*UAP at varying concentrations of GlcNAc-1-P reveals a mixed mode of competition (K_i not calculated). The concentrations of compound **1** used: open circles 300 μM, open squares 100 μM, open triangles 30 μM, and filled circle 0 μM.

60 μM (Figure 2G), while the mixed mode of inhibition observed with GlcNAc-1-P did not allow an apparent K_i to be calculated (Figure 2H).

Compound 1 Binds *Tb*UAP in a Unique Allosteric Site. To gain further insight into the binding interactions with *Tb*UAP, cocrystallization with various ligands was attempted. We were unable to obtain suitable diffraction quality crystals in the presence of substrates or product, but cocrystallization with **1** alone resulted in crystals that diffracted to high resolution. The bound complex was refined against synchrotron diffraction data to 1.75 Å (Table 3), revealing clear density for the inhibitor at a site distinct from the active site (Figure 3A). This represents the

first UAP structure from *T. brucei* or indeed any protist. In common with other eukaryotic UAP structures,[11,12] the *Tb*UAP structure consists of a central pyrophosphorylase domain of eight β-strands sandwiched by eight α-helices in a Rossmann fold,[13] which contains the active site, flanked by an N-terminal domain containing the N-terminus (residues 1−62) and additional β-sheets from the central domain (residues 209−231 and 377−396), and a short C-terminal domain. Strikingly, the inhibitor binding site is located away from but facing the active site in a deep hydrophobic cleft formed by the central and C-terminal domain (Figure 3A,B) where it is able to form hydrogen bonds between the amide group of indolin-2-one and the Gly44 carboxyl group at a distance of 2.8 Å and between the carboxyl group of indolin-2-one with the amide group of Asp46 at a distance of 2.8 Å, as well as a number of hydrophobic interactions (Figure 3C,D). In the published structures of *Candida albicans* UAP (*Ca*UAP) there is distinct movement in the N-terminal domain between the apo-form and the GlcNAc-1-P or UDP-GlcNAc bound forms,[12] consistent with an induced-fit movement that closes the entrance to the binding site upon substrate binding. The inhibitor makes contact with residues on the opposite face of a glycine-rich loop that moves to make contact with the uridine of bound UDP-GlcNAc (Figure 3B), and *Tb*UAP adopts a conformation that most closely resembles the apo-*Ca*UAP structure (2YQC, RMSD 2.2 Å) and least resembles the *Ca*UAP structure with UDP-GlcNAc bound (2YQJ, RMSD 2.7 Å). Thus, **1** appears to act as an allosteric competitive inhibitor of UTP by stabilizing the N-terminal domain and uridine-binding loop in a conformation that prevents the binding of UTP yet does not occupy the UTP binding site itself. Allosteric regulation of *Tb*UAP activity is consistent with reports that *Giardia lamblia* UAP activity is altered *in vivo* by the allosteric binding of the metabolite glucosamine-6-phosphate, although in that case binding caused an increase in activity.[14]

Compound 1 Structure−Activity Relationships. The conformation of the allosteric site is such that only the (*R*)-enantiomer of **1** can bind, and it is likely that the kinked shape of the molecule is crucial for its shape-complimentarity to the pocket. The benzo[1,3]dioxole moiety is deeply buried, making close contact with Ala397 and Gly232 at the bottom of the cleft (Figure 3C,D). Consistent with this binding mode, the commercial structural analogue of **1** that lacks the benzo[1,3]dioxole moiety does not inhibit *Tb*UAP1, and even replacement of the bridging methylene with ethylene is not tolerated (Table 2). The indolin-2-one sits at the top of the cleft, with the unsubstituted edge exposed to solvent and the methyl and bromide substituents on making contact with Ala239, Met370, Lys371, and Ala367 (Figure 3C,D). Removal of the bromine reduces potency >6-fold, and removal of both the bromine and methyl groups reduces potency ≥10-fold (Table 2). The observed SAR for the commercial analogues is consistent with the contacts observed in the crystal structure.

Allosteric Binding Site Is Unique to *Tb*UAP1. Comparison of the *Tb*UAP-**1** structure with the structure of *Hs*UAP[11] revealed that the central catalytic domains are structurally similar (RMSD 1.4 Å), but that the flanking N-terminal and C-terminal domains occupy different positions (maximum Cα atom shift is 9.5 Å, Figure 3E). The inhibitor binding cleft formed by the central and C-terminal domain is wider (10.3 Å versus 7.7 Å) and shallower (10.9 Å versus 17.4 Å) due to both significant movement of the α-helices and nonconservative substitutions. Critically, the substitution of Gly232 in *Tb*UAP with Asp221 in *Hs*UAP blocks the benzo[1,3]dioxole binding site, and the substitution of Ala239 in *Tb*UAP with Arg228 in *Hs*UAP blocks the entrance to the cleft by

Table 1. Surface Plasmon Resonance Parameters[a]

ligand(s)	enzyme	k_a (M^{-1} s^{-1})	k_d (s^{-1})	K_D (μM)	R_{max} (RU)
UTP	*Tb*UAP	N/A	N/A	83.1 ± 0.5	15.20 ± 0.02
GlcNAc-1-P	*Tb*UAP	ND	ND	ND	ND
1	*Tb*UAP	4.13 ± 0.10	0.11 ± 0.10	2.58 ± 0.07	30.67 ± 0.20
1 + 500 μM UTP	*Tb*UAP	2.24 ± 0.04	0.21 ± 0.03	9.30 ± 0.09	10.21 ± 0.05
1 + 100 μM GlcNAc-1-P	*Tb*UAP	5.71 ± 0.02	0.13 ± 0.04	2.35 ± 0.03	26.16 ± 0.02
UTP	*Hs*UAP	ND	ND	ND	ND
GlcNAc-1-P	*Hs*UAP	*b*	*b*	*b*	~35
1	*Hs*UAP	ND	ND	ND	ND

[a]N/A: kinetic parameters are not available due to fast on-rate and off-rate; affinity was determined using equilibrium fit. ND: binding not detected.
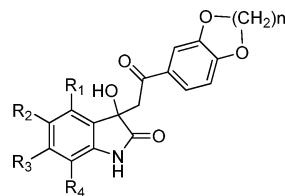[b]No fit was possible due to complex binding kinetics.
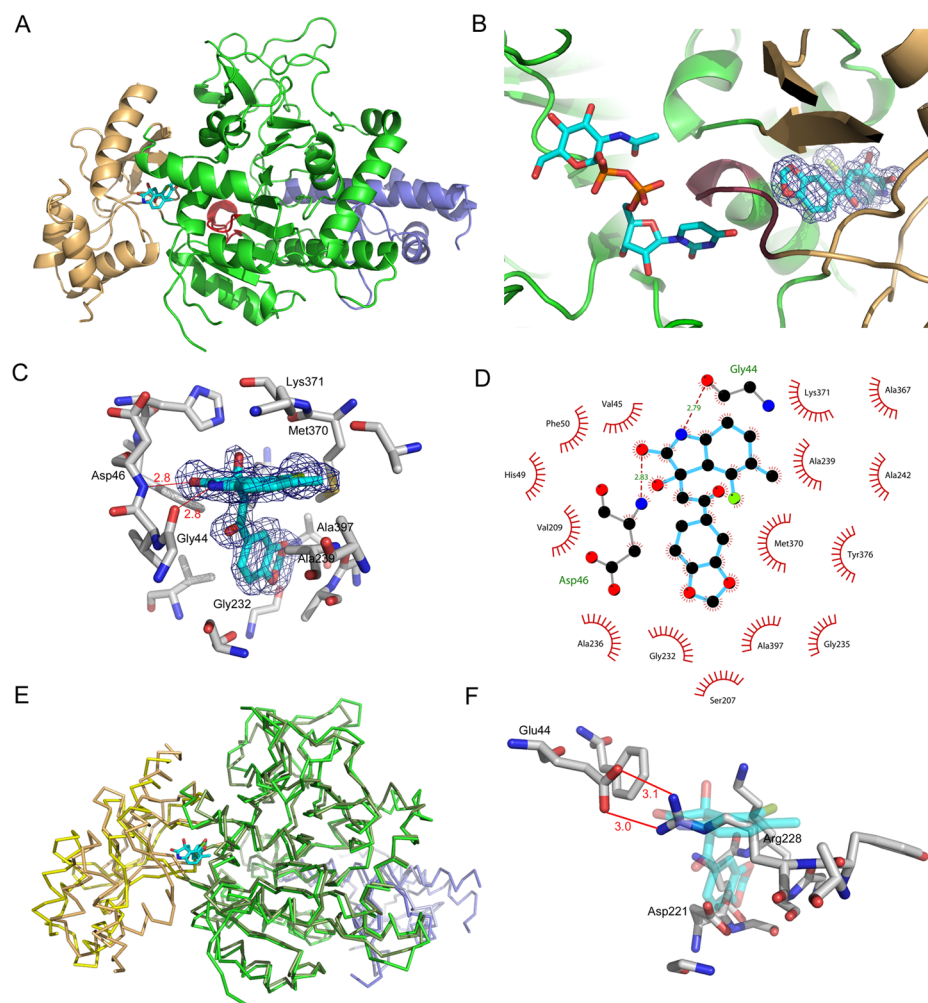
Figure 3. Structure of *Tb*UAP in complex with **1**. (A) Overview of the *Tb*UAP-**1** structure (PDB ID 4bqh), which is composed of an N-terminal domain (beige), a central domain (green) containing the active site (nucleotide binding motif, red), and a C-terminal domain (blue). **1** (light blue) binds at an allosteric site. (B) **1** forms close contacts with a loop (PGGNG, dark red) between the N-terminal and central domain on the opposite face to the UDPGlcNAc binding site. The $2F_0 - F_c$ density of **1** is contoured at 1σ (dark blue mesh). Alignment of the *Tb*UAP central domain with the *Ca*UAP structure 2YQS[12] was used to model the UDPGlcNAc position. (C) Binding interactions of **1** with *Tb*UAP, with the $2F_0 - F_c$ density of **1** displayed. (D) Schematic of the key interactions in the *Tb*UAP-**1** complex. (E) C-α trace showing that the allosteric binding site of *Hs*UAP is wider and flatter due to movement of the N-terminal domain. (F) Binding interactions in the modeled *Hs*UAP-**1** complex showing steric clashes produced by nonconservative substitution. Alignment of the *Tb*UAP central domain with the *Hs*UAP structure 1JV1[11] (gray) was used to model the binding of **1** (blue, transparent).

forming a salt bridge with Glu44 (Figure 3F). The structural data thus explain the observed selectivity of **1**.

Compound 1 Inhibits Growth in *T. brucei* Cultures. We determined that **1** has an EC$_{50}$ of 30 μM against cultured *T. brucei* (data not shown), a surprisingly small drop-off in potency compared to the IC$_{50}$ of 30 μM recorded against the recombinant

T. brucei enzyme. To assess the mode of action of **1**, we determined its potency against a *Tb*UAP conditional null mutant (*Tb*UAP-cKO) cell line in culture. The conditional null mutant, where both allelic copies of *Tb*UAP are replaced by drug resistance cassettes, expresses *Tb*UAP from an ectopic copy under the control of tetracycline.[8] The *Tb*UAP-cKO cell line is

D

dx.doi.org/10.1021/cb400411x | *ACS Chem. Biol.* XXXX, XXX, XXX−XXX

Table 2. Structures of Selected Commercial Analogues of 1[a]

compd	n	R[1]	R[2]	R[3]	R[4]	inhibition at 100 μM (%)
1	1	Br	Me	H	H	65
3	2	H	Me	H	H	0
4	1	H	Me	H	H	27
5	1	Cl	H	Cl	H	25
6	1	H	H	Me	Me	28
7	1	H	H	H	Me	13

[a]The binding mode of **1** observed in the *Tb*UAP-**1** crystal structure is consistent with the observed structure−activity relationships.

viable in the presence of tetracycline (permissive conditions), where expression of *Tb*UAP occurs, although the cellular levels of UDP-GlcNAc are reduced (16 pmol/1×10^7 cells) compared to the wild type (80 pmol/1×10^7 cells) due to a reduced level of *Tb*UAP expression. The EC$_{50}$ was not significantly changed between the wild-type and *Tb*UAP-cKO cell line, suggesting that the cytotoxicity of the compound is not driven by inhibition of *Tb*UAP. To assess whether **1** was able to inhibit *Tb*UAP in *T. brucei* cells, we treated wild-type cells with 100 μM **1** ($3 \times$ IC$_{50}$) or DMSO for 3 h and measured the intracellular levels of sugar nucleotides by LC−MS/MS.[15,16] No significant difference in the level of sugar nucleotides was observed between the treated and untreated samples. Taken together, these data suggest that the observed cytotoxicity of **1** against cultured *T. brucei* is due to an off-target effect and not through the inhibition of *Tb*UAP.

Concluding Remarks. We have discovered a novel UTP-competitive inhibitor of *T. brucei* UAP that displays good selectivity for the parasite enzyme over the human homologue due to binding at a previously unidentified allosteric binding site. While the current inhibitor is of modest potency and the *in vivo* parasite toxicity is likely to be due to off-target effects, the structural data will facilitate the design and synthesis of more potent compounds that may have therapeutic potential. A potential drawback to the targeting of an allosteric site rather than the active site is that resistance may occur more readily due to lack of selective pressure to maintain interactions with the enzyme substrate. However, as the binding site is formed by a hinge region between two domains that undergo induced-fit movement during the catalytic cycle, such substitutions may not be tolerated.

Our studies have revealed that the UAP mechanism is strictly sequentially ordered, but that the order of substrate binding is reversed between the parasite and human enzyme. As the parasite UAP strictly binds UTP first, it follows that UTP-competitive inhibitors may show selectivity for the parasite enzyme over the human enzyme. Traditional sequence- and structure-based drug discovery approaches did not predict that species specificity would be readily achievable due to the high level of conservation of active site residues, highlighting the importance of biophysical studies in target evaluation.

■ METHODS

Cloning, Expression, and Purification of *Hs*UAP. *Homo sapiens* UAP-AX1 (*Hs*UAP, NP_003106) was amplified by PCR from cDNA (OriGeneTechnologies) using the primers 5′-GGAATTC<u>CATAT-GAACATTAATGACCTC</u>-3′ (*Nde*I site underlined) and 5′-CGC-

<u>GGATCC</u>CTCGAGTCAAATACCA-3′ (*Bam*HI site underlined) and inserted into pET15b-pp (a modified pET15b with the thrombin site replaced with PreScission protease) using the *Nde*I and *Bam*HI RE sites to give the plasmid pET15b-pp-*Hs*UAP-AX1. Recombinant *Hs*UAP-His$_6$ was expressed in BL21 (DE3) *E. coli* from the vector pET15b-pp-*Hs*UAP-AX1 and purified in a single step using Ni^{2+} affinity chromatography using the same condition as reported for *Tb*UAP-His$_6$.[8] The identity of recombinant *Hs*UAP-AX1 was confirmed by tryptic mass finger printing (Mascot score 1814, 88% sequence coverage). Purified recombinant UAPs were stored in 50 mM Tris-HCl pH 7.5, 10 mM MgCl$_2$, and 10% glycerol at −80 °C prior to use.

Expression of *Tb*UAP for Activity Assays. Recombinant *Tb*UAP-His$_6$ for activity assay was cloned from *T. brucei*, expressed from the plasmid pET15b-pp-*Tb*UAP in *Escherichia coli* BL21 (DE3), and purified in a single step using Ni^{2+} affinity chromatography as reported previously.[8] For crystallization trials, the *Tb*UAP gene was cut from the pET15b-PP-*Tb*UAP1 plasmid and cloned into a *Bam*HI digested pGEX-6P-1 vector (GE Healthcare). The resulting plasmid, pGEX-6P-1-*Tb*UAP, encodes a glutathione-*S*-transferase (GST) fusion *Tb*UAP separated by a PreScission protease cleavage site.

High-Throughput Screening of *Tb*UAP. The *Tb*UAP high-throughput screen was performed using a Dundee Drug Discovery Unit in-house diverse compound collection of 63,362 molecules[17] against a discontinuous coupled colorimetric assay. The assay was performed at RT in 384-well plates in a final reaction volume of 50 μL in reaction buffer (50 mM Tris pH 7.5, 10 mM MgCl$_2$, 2% v/v glycerol, 1 mM dithiothreitol, 0.1 mg mL^{-1} bovine serum albumin, 1 unit mL^{-1} *E. coli* pyrophosphatase) supplemented with 30 μM UTP, 100 μM GlcNAc-1-P, 0.5 nM recombinant *Tb*UAP, and 30 μM test compound with a final concentration 1% DMSO. Test compounds in 0.5 μL of DMSO were transferred to the plates prior to the addition of recombinant *Tb*UAP in 24.5 μL of reaction buffer. The reaction was initiated by the addition of the substrates UTP and GlcNAc-1-P in 25 μL of reaction buffer and allowed to proceed for 8 min before termination by the addition of 50 μL of Biomol Green (0.03% malachite green, 0.2% w/v ammonium molybdate, 0.5% Triton X-100 in 0.7 M HCl). The signal was allowed to develop for a minimum of 30 min before the absorbance of each well was read at 650 nm. The assay gave a robust average Z′ of 0.8 ± 0.1, with an average coefficient of variance of 1−3% and signal/background of 2.5 ± 0.3 based on the inclusion of high (uninhibited) and low (no enzyme) control wells in each of the 183 assay plates.

Compounds with ≥25% inhibition in the screen (100, 0.16% hit rate) were cherry picked and confirmed by retesting, with a 73% confirmation rate (Supplementary Table S1). Confirmed hits were tested for potency against the pyrophosphatase by modifying the discontinuous coupled colorimetric assay to include 5 mM inorganic pyrophosphate, and compounds showing >15% difference between the pyrophosphatase and coupled assay (Supplementary Table S2) were considered *Tb*UAP hits (12, 0.02% hit rate). The *Tb*UAP hits were repurchased, and 10-point inhibitor IC$_{50}$ curves were determined using the discontinuous coupled colorimetric assay and fitting the dose−response curve to a four-parameter fit in ActivityBase XE (IDBS).

High pH Anion Exchange Chromatography. The inhibition of *Tb*UAP and *Hs*UAP was measured using high pH anion exchange chromatography (HPAEC) to follow the conversion of UTP to UDP-GlcNAc by *Tb*UAP. The reaction buffer (50 mM Tris pH 7.5, 10 mM MgCl$_2$, 2% v/v glycerol, 1 mM dithiothreitol, 0.1 mg mL^{-1} bovine serum albumin, 1% DMSO) was supplemented with 25 μM UTP, 40 μM GlcNAc-1-P, and 25 ng *Tb*UAP or 75 ng *Hs*UAP. The reaction (100 μL) was incubated at 30 °C for 30 min with or without inhibitor, quenched by the addition of 10 μL of 0.1 M NaOH, and then subjected to HPAEC chromatography on a CarboPac PA-1 column (Dionex) using conditions adapted from Tomiya et al.[18] The eluent was monitored at 260 nm, and peaks were assigned by comparison to commercial standards. The IC$_{50}$ value was calculated using a four-parameter fit of eight-point potency curves derived from three independent experiments.

Competition Studies. The kinetic parameters for *Tb*UAP were determined in the presence of different concentrations of substrates and inhibitor using the discontinuous coupled colorimetric assay described above. The reaction was performed either at fixed concentration of

E

dx.doi.org/10.1021/cb400411x | *ACS Chem. Biol.* XXXX, XXX, XXX−XXX

40 μM GlcNAc-1-P and 5−640 μM of UTP in the presence of 0−300 μM **1**, or at a fixed concentration of 25 μM UTP and 4−500 μM GlcNAc-1-P in the presence of 0−300 μM **1**, and the data were fitted to the Michaelis−Menten equation and displayed as a double reciprocal plot. The calculated apparent $K_m(UTP)^{app}$ in the presence of a range of concentrations of **1** was used to calculate K_i by plotting $K_m(UTP)^{app}$ against [I] to solve the equation $K_m^{app} = (K_m/K_i)[I] + K_m$.

Surface Plasmon Resonance. Recombinant *Tb*UAP and *Hs*UAP were chemically biotinylated and captured on a streptavidin surface of a Biacore T100 instrument (GE-Healthcare) at densities ∼6,000−7,000 RU. To stabilize captured proteins over time all experiments were run at 4 °C. Ligands were injected over captured proteins at flow rate 30 μL min^{-1} in running buffer (50 mM Tris pH 7.5, 150 mM NaCl, 10 mM MgCl$_2$, 0.05% Tween 20, 1 mM DTT, 3% DMSO), with each compound injected in duplicates in concentration series adjusted specifically for each ligand; UTP was injected at 2-fold concentration series (3.9−500 μM), GlcNAc-1-P at 3-fold concentration series (9 nM to 20 μM), and **1** at 3-fold concentration series (69 nM to 500 μM). Association was measured for 30 s and dissociation for 30−300 s depending on the off-rate. For competition studies, 500 μM UTP or 100 μM Glc-NAc-1-P was added to the running buffer. All data were double referenced for blank injections of buffer and biotin-blocked Streptavidin surface. Scrubber 2 (BioLogic Software) was used to process and analyze the data.

Expression and Purification of *Tb*UAP for Crystallography. Recombinant *Tb*UAP-GST was expressed from the plasmid pGEX-6P-1-*Tb*UAP in *E. coli* BL21 (DE3) pLysS. Cells were grown in LB at 37 °C to an OD$_{600}$ of 0.8 and cooled to RT, and protein expression was induced with 250 μM isopropyl-β-D-thiogalactopyranoside for 20 h. Cells were harvested by centrifugation at 3500 × *g* at 4 °C for 30 min, resuspended in buffer A (25 mM Tris pH 7.5, 150 mM NaCl) in the presence of 10 mg mL^{-1} DNase, a protease inhibitor cocktail (Roche) and 0.5 mg mL^{-1} lysozyme), lysed on a EmulsiFlex-C3 homogenizer at 20 kpsi (Avestin), and centrifuged at 40,000 × *g* for 30 min. The supernatant was incubated with prewashed glutathione sepharose beads (GE Healthcare) at 4 °C on a rotating platform for 2 h, and the beads were isolated by centrifugation at 1000 × *g* for 3 min and washed with buffer A four times. *Tb*UAP was cleaved from the GST tag by treatment with PreScission protease in the same buffer at 4 °C on a rotating platform for 18 h, and the released protein was further purified on a Superdex75 gel filtration column (2.6 cm × 60 cm) (Amersham Biosciences) with 1.0 mL min^{-1} buffer A. The fractions were verified by SDS-PAGE, pooled, and concentrated to 15 mg mL^{-1} using a 10-kDa cutoff Vivaspin concentrator (GE Healthcare).

Crystallization, Data Collection, and Structure Determination. Crystallization was conducted using the sitting-drop vapor diffusion method at RT, where each drop contained 0.5 μL of *Tb*UAP1 solution (15 mg mL^{-1} in buffer A) with an equal volume of the mother liquor. To obtain the *Tb*UAP1-**1** complex, the protein was incubated with 0.495 M compound at 4 °C for 30 min before setting up crystal trays. The complex crystallized after 4−5 days in the space group C222$_1$ from a mother liquor containing 25% PEG3350, 0.2 M (NH$_4$)$_2$SO$_4$, 0.1 M Bis-Tris pH 5.5. Crystals were cryo-protected in this solution supplemented with 15% glycerol. X-ray data were collected at the I-24 (microfocus) beamline of the Diamond (U.K.) synchrotron and processed with HKL2000.[19] The phase problem was solved by the automated molecular replacement pipeline BALBES;[20] REFMAC[21] was used for further refinement and iterated with model building using COOT.[22] Detailed crystallographic parameters are given in Table 3. The model for ligands was not included until their conformations were fully defined by unbiased $|F_o| − |F_c|$, φ_{calc} electron density maps. Ligand structures and topologies were generated by PRODRG.[23] Images were generated with PyMol[24] and LigPlot$^+$.[25] The final structure coordinates and structure factors are available in the PDB (4bqh and r4bqhsf, respectively).

Trypanosoma brucei **Growth Inhibition.** The potency of **1** against cultured *T. brucei* was determined using a standard 3-day Alamar blue assay as described previously.[26] Assays were conducted using the Lister 427 single marker cell line[27] or a *Tb*UAP conditional null mutant[8] grown in HMI9-T.[28] The EC$_{50}$ values were calculated from 8-point potency curves in triplicate.

Table 3. Details of Diffraction Data Collection and Structure Refinement for *Tb*UAP1 + 1^a

resolution (Å)	25.00 (1.75)
space group	C222$_1$
unit cell	
a (Å)	59.9
b (Å)	103.0
c (Å)	187.1
no. of reflections	334133
no. of unique reflections	58590
I/σ (I)	13.6 (4.5)
completeness (%)	99.7 (99.2)
redundancy	5.7 (5.4)
R_{merge} (%)	7.3 (34.9)
RMSD from ideal geometry	
bond dist (Å)	0.01
bond angle (deg)	1.30
R_{work} (%)	18.9
R_{free} (%)	21.9
no. of residues	541
no. of water molecules	408
B factors (Å^2)	
overall	19.5
protein	18.8
ligand	13.6
water	26.9

^{a}Values in brackets are for the highest resolution shell. All measured data were included in structure refinement.

Sugar Nucleotide Analysis. *T. brucei* Lister 427 single marker cells grown in HMI9-T[28] were treated with 100 μM of **1** in 0.1% DMSO or a 0.1% DMSO control for 3 h. Cells were harvested by centrifugation, the intracellular sugar nucleotides were extracted, and their levels were quantified by LC−MS/MS analysis as described previously.[15,16]

■ ASSOCIATED CONTENT

Ⓢ Supporting Information

Further details of the 73 initial hits (Table S1) and the 30 commercially available compounds (Table S2). This material is available free of charge via the Internet at http://pubs.acs.org.

Accession Codes

The *Tb*UAP-**1** structure coordinates (4bqh) and structure factors (r4bqhsf) are available in the PDB.

■ AUTHOR INFORMATION

Corresponding Author

*E-mail: m.a.j.ferguson@dundee.ac.uk.

Notes

The authors declare no competing financial interest.

■ ACKNOWLEDGMENTS

■ REFERENCES

(1) Simarro, P., Diarra, A., Ruiz Postigo, J., Franco, J., and Jannin, J. (2011) The Human African Trypanosomiasis Control and Surveillance Programme of the WHO 2000−2009: The Way Forward. *PLoS Negl. Trop. Dis. 5*, e1007.

F

dx.doi.org/10.1021/cb400411x | *ACS Chem. Biol.* XXXX, XXX, XXX−XXX

(2) Frearson, J. A., Wyatt, P. G., Gilbert, I. H., and Fairlamb, A. H. (2007) Target assessment for antiparasitic drug discovery. *Trends Parasitol.* 23, 589−595.

(3) Chang, T., Milne, K. G., Guther, M. L. S., Smith, T. K., and Ferguson, M. A. J. (2002) Cloning of *Trypanosoma brucei* and *Leishmania major* genes encoding the GlcNAc-phosphatidylinositol de-*N*-acetylase of glycosylphosphatidylinositol biosynthesis that is essential to the African sleeping sickness parasite. *J. Biol. Chem.* 277, 50176−50182.

(4) Nagamune, K., Nozaki, T., Maeda, Y., Ohishi, K., Fukuma, T., Hara, T., Schwarz, R. T., Sutterlin, C., Brun, R., Reizman, H., and Kinoshita, T. (2000) Critical roles of glycosylphosphatidylinositol for *Trypanosoma brucei. Proc. Natl. Acad. Sci. U.S.A.* 97, 10336−10341.

(5) Lillico, S., Field, M. C., Blundell, P., Coombs, G. H., and Mottram, J. C. (2003) Essential role for GPI-anchored proteins in African trypanosomes revealed using mutants deficient in GPI8. *Mol. Biol. Cell* 14, 1182−1194.

(6) Roper, J. R., Guther, M. L. S., Milne, K. G., and Ferguson, M. A. J. (2002) Galactose metabolism is essential for the African sleeping sickness parasite *Trypanosoma brucei. Proc. Natl. Acad. Sci. U.S.A.* 99, 5884−5889.

(7) Turnock, D. C., Izquierdo, L., and Ferguson, M. A. J. (2007) The *de novo* synthesis of GDP-fucose is essenatial for flagellar adhesion and cell growth in *Trypanosoma brucei. J. Biol. Chem.* 282, 28853−28863.

(8) Stokes, M. J., Guther, M. L. S., Turnock, D. C., Prescott, A. R., Martin, K. L., Alphey, M. S., and Ferguson, M. A. J. (2008) The synthesis of UDP-*N*-acetylglucosmine is essential for bloodstream form *Trypanosoma brucei in vitro* and *in vivo* and UDP-*N*-acetylglucosamine starvation reveals a hierarchy in parasite protein glycoslyation. *J. Biol. Chem.* 283, 16147−16161.

(9) Denton, H., Fyffe, S., and Smith, T. K. (2010) GDP-mannose pyrophosphorylase is essential in the bloodstream form of *Trypanosoma brucei. Biochem. J.* 425, 603−614.

(10) Bandini, G., Marino, K., Guther, M. L. S., Wernimont, A. K., Kuettel, S., Qiu, W., Afzal, S., Kelner, A., Hui, R., and Ferguson, M. A. J. (2012) Phosphoglucomutase is absent in *Trypanosoma brucei* and redundantly substituted by phosphomannomutase and phospho-*N*-acetylglucosamine mutase. *Mol. Microbiol.* 85, 513−534.

(11) Peneff, C., Ferrari, P., Charrier, V., Taburet, Y., Monnier, C., Zamboni, V., Winter, J., Harnois, M., Fassy, F., and Bourne, Y. (2001) Crystal structures of two human pyrophophorylase isoforms in complexes with UDPGlc(Gal)NAc: role of the alternative spliced insert in the enzyme oligomeric assembly and active site architecture. *EMBO J.* 20, 6191−6202.

(12) Maruyama, D., Nishitani, Y., Nonaka, T., Kita, A., Fukami, T. A., Mio, T., Yamada-Okabe, H., Yamada-Okabe, T., and Miki, K. (2007) Crystal Structure of uridine-diphospho-*N*-acetylglucosamine pyrophosphorylase from *Candida albicans* and catalytic reaction mechanism. *J. Biol. Chem.* 282, 17221−17230.

(13) Rao, S., and Rossmann, M. (1973) Comparison of super-secondary structures in proteins. *J. Mol. Biol.* 76, 241−256.

(14) Bulik, D. A., Ophem, P. v., Manning, J. M., Shen, Z., Newbrug, D., and Jarroll, E. L. (2000) UDP-*N*-Acetylglucosamine pyrophosphorylase, a key enzyme in encisting *Giardia*, is allosterically regulated. *J. Biol. Chem.* 275, 14722−14728.

(15) Urbaniak, M. D., Turnock, D. C., and Ferguson, M. A. J. (2006) Characterisation of galactose starvation in a bloodstream form *Trypanosoma brucei* UDP-glucose 4′-epimerase conditional null mutant. *Eukaryotic Cell* 5, 1906−1913.

(16) Turnock, D. C., and Ferguson, M. A. J. (2007) Sugar nucleotide pools of *Trypanosoma brucei, Trypanosoma cruzi*, and *Leishmania major. Eukaryotic Cell* 6, 1450−1463.

(17) Brenk, R., Schipani, A., James, D., Krasowski, A., Gilbert, I. H., Frearson, J. A., and Wyatt, P. G. (2008) Lessons learnt from assembling screening libraries for drug discovery for neglected diseases. *ChemMedChem* 3, 435−444.

(18) Tomiya, N., Ailor, E., Lawrence, S. M., Bettenbaugh, M. J., and Lee, Y. C. (2002) Determination of nucleotides and sugar nucleotides involved in protein glycosylation by high-perforamnce anion-exchange chromatography: Sugar nucleotide contents in cultured insect cells and mammalian cells. *Anal. Biochem.* 293, 129−137.

(19) Otwinowski, Z., and Minor, A. (1997) Processing of X-ray diffraction data collected in oscillation mode. *Methods Enzymol.*, 307−326.

(20) Long, F., Vagin, A. A., Young, P., and Murshudov, G. N. (2008) BALBES: a molecular-replacement pipeline. *Acta Crystallogr., Sect. D: Biol. Crystallogr.* 64, 125−132.

(21) Murshudov, G. N., Vagin, A. A., and Dodson, E. J. (1997) Refinement of macromolecular structures by the maximum-likelihood method. *Acta Crystallogr., Sect. D: Biol. Crystallogr.* 53, 240−255.

(22) Emsley, P., and Cowtan, K. (2004) Coot: model-building tools for molecular graphics. *Acta Crystallogr., Sect. D: Biol. Crystallogr.* 60, 2126−2132.

(23) Schuettelkopf, A. W., and van Aalten, D. M. F. (2004) PRODRG: a tool for high-throughput crystallography of protein-ligand complexes. *Acta Crystallogr.* D60, 1355−1363.

(24) DeLano, W. L. (2004) Use of PYMOL as a communication tool for molecular science. *Abstr. Pap. Am. Chem. Soc.* 228, 030-CHED.

(25) Laskowski, R. A., and Swindells, M. B. (2011) LogPlot+: multiple ligand protein interaction diagrams for drug discovery. *J. Chem. Inf. Model.* 51, 2778−2786.

(26) Urbaniak, M. D., Tabudravu, J. N., Msaki, A., Matera, K. M., Brenk, R., Jaspars, M., and Ferguson, M. A. J. (2006) Identification of novel inhibitors of UDP-Glc 4′-epimerase, a validated drug target for African sleeping sickness. *Bioorg. Med. Chem. Lett.*, 5744−5747.

(27) Wirtz, E., Leal, S., Ochatt, C., and Cross, G. A. M. (1999) A tightly regulated inducible expression system for conditional gene knock-outs and dominant-negative genetics in *Trypanosoma brucei. Mol. Biochem. Parasitol.* 99, 89−101.

(28) Urbaniak, M. D., Martin, D. M. A., and Ferguson, M. A. J. (2013) Global comparative SILAC phosphoproteomics reveals differential phosphorylation is widespread between the procyclic and bloodstream form lifecycle stages of *Trypanosoma brucei. J. Proteome Res.* 12, 2233−2244.